AIP ADVANCES **6**, 065125 (2016)

Cold welding of organic light emitting diode: Interfacial and contact models

J. Asare,[1,2] S. A. Adeniji,[3] O. K. Oyewole,[1,2,4] B. Agyei-Tuffour,[3] J. Du,[5,6,7] E. Arthur,[3,4] A. A. Fashina,[1] M. G. Zebaze Kana,[1,4] and W. O. Soboyejo[3,6,7,a]
[1]*Department of Theoretical and Applied Physics, African University of Science and Technology, Km 10 Airport Road, Abuja, Federal Capital Territory, Nigeria*
[2]*Department of Physics, Baze University, Plot 686 Cadastral Zone C00, Kuchigoro, Abuja, Federal Capital Territory, Nigeria*
[3]*Department of Materials Science and Engineering, African University of Science and Technology, Km 10 Airport Road, Abuja, Federal Capital Territory, Nigeria*
[4]*Department of Materials Science and Engineering, Kwara State University, Malete, Kwara State, Nigeria*
[5]*Department of Mechanical & Nuclear Engineering, Pennsylvania State University, University Park, Pennsylvania, USA*
[6]*Department of Mechanical and Aerospace Engineering, Olden Street, Princeton University, New Jersey, USA*
[7]*Princeton Institute of Science and Technology of Materials (PRISM), 70 Prospect Street, Princeton, New Jersey, 08544, USA*

(Received 27 March 2016; accepted 20 June 2016; published online 28 June 2016)

This paper presents the results of an analytical and computational study of the contacts and interfacial fracture associated with the cold welding of Organic Light Emitting diodes (OLEDs). The effects of impurities (within the possible interfaces) are explored for contacts and interfacial fracture between layers that are relevant to model OLEDs. The models are used to study the effects of adhesion, pressure, thin film layer thickness and dust particle modulus (between the contacting surfaces) on contact profiles around impurities between cold-welded thin films. The lift-off stage of thin films (during cold welding) is then modeled as an interfacial fracture process. A combination of adhesion and interfacial fracture theories is used to provide new insights for the design of improved contact and interfacial separation during cold welding. The implications of the results are discussed for the design and fabrication of cold welded OLED structures. © *2016 Author(s). All article content, except where otherwise noted, is licensed under a Creative Commons Attribution (CC BY) license (http://creativecommons.org/licenses/by/4.0/).* [http://dx.doi.org/10.1063/1.4955141]

I. INTRODUCTION

There has been significant interest in the fabrication of organic electronic structures using cold welding techniques.[1–6] Cold welding or cold pressure welding has been described as a process by which clean surfaces are brought together to achieve intimate contact, and thereby form strong bonds at the resulting interfaces.[7] It has attracted widespread attention due to its potential for low-cost fabrication of organic electronic devices.[8]

The initial step in cold welding involves bringing together the surfaces of two different thin film materials at room temperature.[9] In most cases, the contact occurs around dust particles that are present in the clean room environment[10] These include materials such as silicone, silicon, silica and organic materials. The contacts are enhanced by the application of pressure,[3,11–15] which is often applied through compliant materials such as poly-di-methyl-siloxane (PDMS). Such compliant

[a]Correspondence to Professor Wole Soboyejo, Department of Mechanical and Aerospace Engineering, Engineering Quadrangle Room D40B, Princeton, NJ08544, USA. Phone: +1-609-258-5609, Fax: +1-609-258-5877; Email: soboyejo@princeton.edu

 ©Author(s) 2016.

layers improve the contacts between the cold welded layers. However, increasing pressure can lead to excessive sink-in of dust particles[15] and the damage of the organic electronic device.[16]

There is, therefore, a need to control the pressure that is applied during the cold welding of organic electronic structures. Similarly, the transfer of one metal film to the other (that occurs during cold welding) requires careful control of the interfacial fracture processes that can occur in any of the interfaces with the organic electronic structures. Also, depending on the interfacial and layer fracture energies, fracture may occur by interfacial or layer fracture, or a combination of both.[17,18]

Prior work on cold welding[8,9,15,19–21,6,16,22] of thin film organic electronics has been carried out by Cao *et al.*[3] Kim *et al.*[4] and Akande *et al.*[2] These studies have identified the role of interfacial impurities in the cold welding of gold-gold and gold-silver thin films that are relevant to OLEDs. They have also focused largely on the effects of stiff impurities on contacts induced by the application of pressure. However, it is quite possible for the moduli of interfacial impurities (silicon, silicon oxide and organic materials) to vary significantly.[23] The adhesion energies and layer dimensions may also affect the surface contacts and pull-off forces associated with the lift off stage of cold welding, which may be considered as an interfacial fracture process, as in recent work on the lamination of organic electronic structures.[3,23–26]

Hence, in this paper, we present the results of a study of the pressure-associated contact and lift-off stages that are associated with the cold welding of Au, Ag and other organic layers used in OLED structures. The effects of impurity Young's moduli are elucidated, along with the role of layer thickness and interfacial adhesion energy. These are explored using finite element models. The paper is divided into five sections. Following the introduction, surface contact and pull-off theories are presented in Section II. The experimental methods are then described in Section III before discussing the results in Section IV. Salient conclusions arising from the study are presented in section V.

II. MODELING

A. Surface contact model

The deformation of a thin film around an interfacial impurity particle can be identified by the displacement of a cantilever beam (Figure 1(a)).[22,27–29] As the beam deflects, the cantilever beam (layer 2) makes contact with the adjacent layer (Layer 1), as shown in Figure 1(b). This results in surface contact that increases with increasing pressure (Figure 1(c)). The corresponding void length, S, also decreases with increasing pressure[16] (Figure 1(c)). Furthermore, the deformation of the sandwiched particle depends on the weight of the film, the pressure of the stamp and the combined (effective) Young's moduli of the particle and the film.

In an effort to model the contact between the two cold-welded layers, Zong *et al.*[30] have shown that the total energy, U_s, stored in the film (due to the bending) is given by:

$$U_s = \frac{6E_f I h^2}{s^3} - \gamma (L - s) a, \tag{1}$$

where a is the width of the film, E_f is the Young's modulus, γ is the adhesion energy between the two cold-welded layers, I is the second moment of area of the beam, h is the height of the particle and L is the length of the beam.

However, before bending, the dust particle (illustrated in Figure 1) can penetrate or indent the film or beam (layer 1), depending on the elastic nature of the dust particle (and that of the beam). Assuming that the dust particle is rigid, the dust particle can be idealized as a rigid indenter that penetrates the film or beam during the application of external pressure. Therefore, the Young's modulus in Equation (1) can be replaced by the effective or combined modulus, E_{eff}, of the dust particle and film:[31,32]

$$\frac{1}{E_{eff}} = \frac{1 - (\upsilon_d)^2}{E_d} + \frac{1 - (\upsilon_f)^2}{E_f} \tag{2}$$

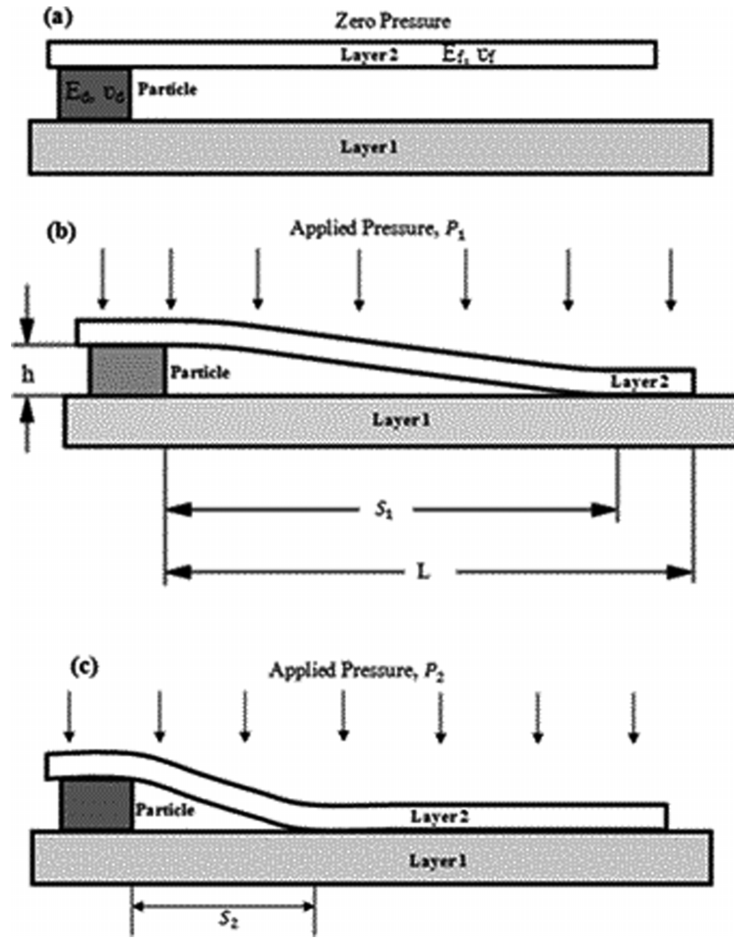

FIG. 1. Elastic deformation of a cold-welded film layer around a particle (a) the layer is in contact with the particle with zero pressure applied (b) small pressure is applied on the film layer (c) additional pressure applied on the film layer. The length, s, of the void decreases with increasing pressure. E_d and E_f represent the Young's moduli of the dust particle and film or beam, respectively. υ_d and υ_f also represent the Poisson's ratios of the dust particle and film or beam, respectively.

$$E_{eff} = \frac{E_d E_f}{E_f[1-(\upsilon_d)^2] + E_d[1-(\upsilon_f)^2]} \tag{3}$$

where E_{eff} is equal to the combined modulus of the film (beam) and the dust particle, E_d and E_f represent the Young's modulus of the dust particle and the film, respectively, υ_d and υ_f represent the Poisson's ratio of the dust particle and the film (beam), respectively. Therefore, Equation (1) becomes (i.e. E_f changes to E_{eff}):

$$U_s = \frac{6E_{eff}Ih^2}{s^3} - \gamma(L-s)\,a. \tag{4}$$

Taking the derivative of Equation (4) with respect to s gives:

$$\frac{dU_s}{ds} = -\frac{18E_{eff}Ih^2}{s^4} + \gamma a. \tag{5}$$

The minimum value of the total energy of the film occurs at a corresponding equilibrium ($dU_s/ds = 0$) value of s. Hence,

$$s = \left(\frac{18E_{eff}Ih^2}{\gamma a}\right)^{\frac{1}{4}} \tag{6}$$

Defining the second moment of area as $I = \frac{at^3}{12}$, Equation (6) can be written as:

$$s = \left(\frac{3E_{eff}t^3h^2}{2\gamma}\right)^{\frac{1}{4}}. \tag{7}$$

where t is the thickness of the film.

Equation (7) can be re-written as:

$$s = \left(\frac{3\left(\frac{E_dE_f}{E_f\left(1-(\upsilon_d)^2\right)+E_d\left(1-(\upsilon_f)^2\right)}\right)t^3h_{eff}^2}{2\gamma}\right)^{\frac{1}{4}} \tag{8}$$

Similarly the contact length can also be written as a function of the applied pressure (the detailed derivation is presented in Appendix) as:

$$\frac{L_c}{L} = 1 - \left(\frac{3\left(\frac{E_dE_f}{E_f\left(1-(\upsilon_d)^2\right)+E_d\left(1-(\upsilon_f)^2\right)}\right)t^3h_{eff}}{2PL^4}\right)^{\frac{1}{4}} \tag{9}$$

where L_c is the contact length, P is the applied pressure, h_{eff} is the effective height of the particle, and L is the length of the structure, as shown Figure 1. The above analytical model (Equation (8)) presented here was verified using the experimental study of adhesion in cold-welded Au–Ag interfaces obtained by Akande *et al.*[2] The results obtained from the finite element simulations were also validated by the experimental results[2] and the predictions obtained from the analytical model (Equation (9)).

Hence, if the geometry and Young's modulus of the film are known, the interfacial adhesion energy between the cold-welded films can, therefore, be determined using force microscopy[33] or interfacial fracture mechanics methods, while the film Young's modulus can be obtained from nano-indentation.[23,34] In the case of non-rigid particles, the applied pressure will also induce the deformation of the trapped particles, as shown schematically in Figures 2(a)-2(c) for stiff, semi-rigid and compliant particles, respectively. In such cases, finite element simulations were used to model the contacts and the deformation of the differential types of particles.

B. Computational modeling of surface contact

In an effort to further understand the surface contact during the pre-cold-welding process and interfacial fracture during lift-off process, several finite element simulations were carried out using the ABAQUS™ software package (Dassault Systèmes Simulia Corporation, Providence, RI). First, the effects of the sandwiched/trapped particles (on surface contact) were simulated. Axisymmetric models were developed for the pre-cold-welding of MEH-PPV onto PDMS substrates (Figure 2). A four-node elemental mesh was used, similar to that in our prior work (Figure 3).[2,3,16,22,35] Fine mesh were used near the particles and the contact surfaces, where the stress and displacement levels were higher. The bottom boundary of the substrate was also fixed to ensure stability during the simulations. A uniform pressure was applied to the top of the stamp to simulate the application of pressure during cold welding. All the materials were assumed to be isotropic. The models were used to simulate the deformation of the layers and particles, as well as the contacts between the layers.

C. Computational modeling of lift-off as a fracture process

The lift-off stage of the cold- welding was modeled as an interfacial fracture process. This involved the interfacial fracture between bi-material pairs with impurity nanoparticles trapped between layers. Nanoparticles with different elastic properties were assumed to be present between

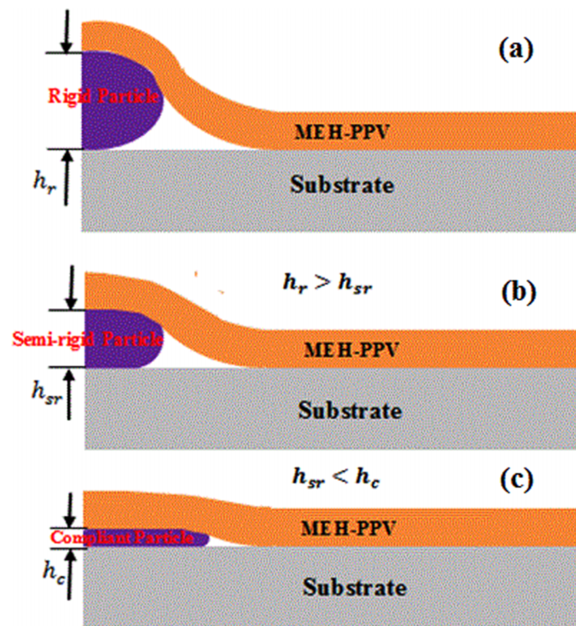

FIG. 2. (a) – (c); Schematic diagram of cold-wedded MEH-PPV on substrate with different sandwich particles. The heights of the rigid, semi-rigid and compliance particles are h_r, h_{sr} and h_c, respectively.

these layered interfaces. Such nanoparticles have been revealed by Akande *et al.*[2] in prior transmission electron microscopy studies of focused ion beam cross sections of cold welded Au-Ag layers. Edge cracks were also idealized between layered interfaces [stamp/layer (top) and/or layer/substrate (bottom) interfaces]. A schematic of the lift-off process is presented in Figure 4.

The energy release rate at the tips of the edge cracks at the interfaces between the cold-welded film and the substrate are given by:[22]

$$G = f\left(\frac{\overline{E}_s}{\overline{E}_f}, \frac{t_s}{t_f}, \frac{d_b}{t_f}, \frac{d_t}{t_f}\right)\frac{\sigma^2 t_f}{\overline{E}_f} \tag{10}$$

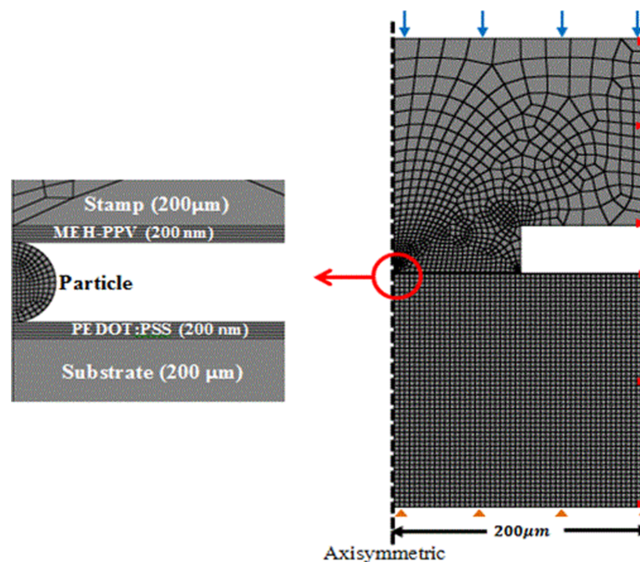

FIG. 3. Geometry and mesh of finite element model of surface contact during cold-welding process (Ref. 22).

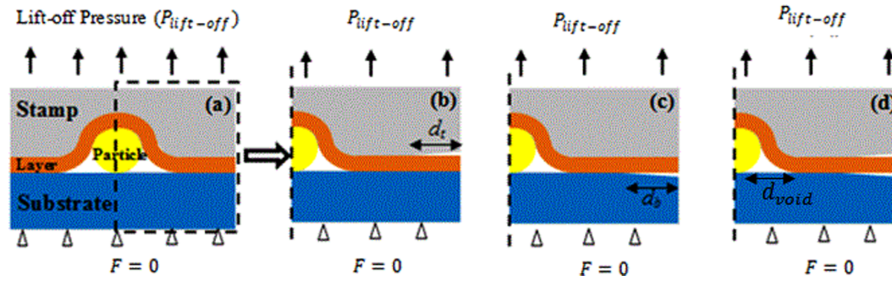

FIG. 4. Schematics of micro scale models of interfacial fracture during the lift-off process of the lamination (a) model of the lift-off process after the press down of the layer on the substrate, (b) axisymmetric model of successful lift-off (note that d_t is the length of a top edge crack), (c) axisymmetric model of unsuccessful lift-off (note that d_s is the length of the bottom edge crack), and (d) axisymmetric model of partial interfacial fracture (note that d_{void} indicates the length of the bottom crack or the crack created by the particle) (Ref. 22).

where $\overline{E}_f = E_f/\left(1 - \nu^2\right)$ and $\overline{E}_s = E_s/\left(1 - \nu^2\right)$ are the plane strain elastic moduli of the film and substrate, d_t and d_b are the lengths of top and bottom interfacial cracks, t_f and t_s are the thicknesses of the film and substrate, respectively, and σ is the lift-off stress.

The simulation of interfacial fracture (during the lift-off stage of the cold-welding process) was carried out using the ABAQUS™ software package (Dassault Systèmes Simulia Corporation, Providence, RI, USA). The interfacial energy release rates at the tips of the edge cracks along stamp/MEH-PPV (top) and MEH-PPV/substrate (bottom) interfaces were computed as J-integrals. Four-node elemental meshes were used. A uniform lift-off pressure was applied to the stamp, while the bottom surface was fixed, as shown in Figure 4. The material properties that were used in the simulations are summarized in Table I. These were obtained largely from the work by Du *et al.*[16] and Akande *et al.*[2]

III. RESULTS AND DISCUSSION

A. Analytical model and verification

TEM images of cold-welded Au–Ag interfaces obtained by Akande *et al.*[2] were used to analyze and estimate the void lengths in the vicinity of carbon dust particles. Carbon steel was the dust particle material that was used to verify the current analytical model since the work reported by Akande *et al.*[2] attributed the presence of carbon steel[2] as one of the dust particle at the cold-welded Au-Ag interfaces.

The void length observed from the theoretical model was compared with quantitative estimates in the presence of carbon steel dust particle between the Ag and Au surfaces observed from Akande *et al.*[2] (Figure 5). The TEM image reveals the presence of dust particles at the cold welded interface. The calculated void lengths are in agreement with the experimental results of Akande *et al.*[2]

TABLE I. Material properties.

Materials	Young Modulus, E / GPa	Poisson's ratio, υ	References
PDMS	0.003	0.48	13,16,36
PEDOT:PSS	1.42	0.3	16
MEH-PPV	11.5	0.3	16
ITO	116	0.35	16,37
Al	70	0.3	38
Carbon steel	205	0.29	39,40
Au	78	0.44	41
Ag	83	0.37	42
Low density polyethylene (LDPE)	0.2	0.3	38,39

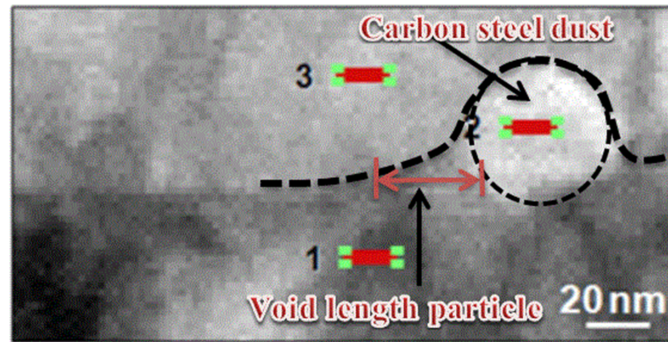

FIG. 5. TEM image showing interfaces of as-deposited and cold-welded Ag–Au thin 1 μm (Ref. 2).

B. Deformation and contact around trapped particles

Unlike prior work by Akande *et al.*,[2] Kim *et al.*[19] and Cao *et al.*,[23] in which the trapped particles were assumed to be rigid, the finite element simulations that were performed in the current work considered the elastic deformation of stiff, semi-rigid and compliant dust particles (i.e. aluminum, plain carbon steel and low density polyethylene, respectively) with Young's moduli of ~70 GPa, 205 GPa and 0.2 GPa,[2,16] respectively. In the case of the rigid particles, the contact lengths predicted by the analytical models are presented in Figure 6(a). The predictions obtained from finite element simulations (that included the actual deformation of the trapped dust particles) are presented in Figure 6(b).

In both cases, the percentage of contact area increased with increasing applied pressure. However, the contact area was lower in the case of the stiffer layers e.g. Aluminum, as expected from prior work that showed that stiffer layers result in reduced contact lengths, for the same applied pressure[2,16,28] In any case, increased pressure resulted in increased contact area, and the percentage of contact approached a plateau, as the pressure was increased, for each bi-material pair (Figure 6(a) and 6(b)).

The contact lengths also increased with increasing particle compliance, due to the increasing deformation of the particles, which resulted ultimately in improved film/surface contact. The modeling of particle deformation is, therefore, important for the modeling of contacts with compliant or trapped nanoparticles. These can give rise to larger open voids, in the case of more rigid particles, or closed elongated voids in the case of more rigid particles, or closed elongated voids in the case of compliant trapped particles. These two types of defects can affect the subsequent lift-off stage of cold welding, when the direction of the loading is reversed. Further details on the pull-off process are presented in the next section.

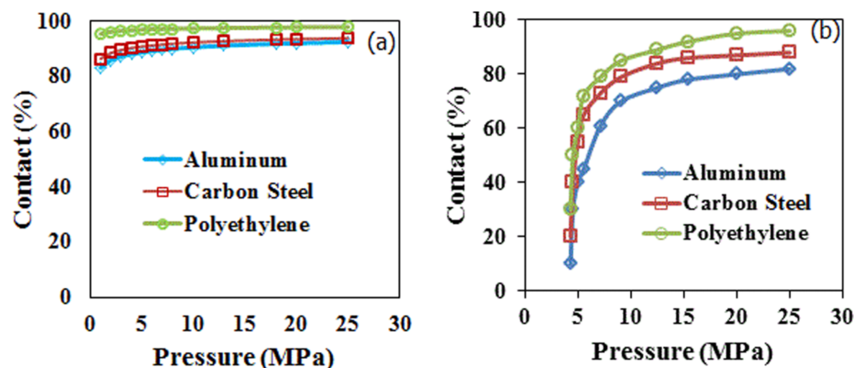

FIG. 6. FEA results effect of pressure on the various contact percentage for (a) analytical and (b) computational models.

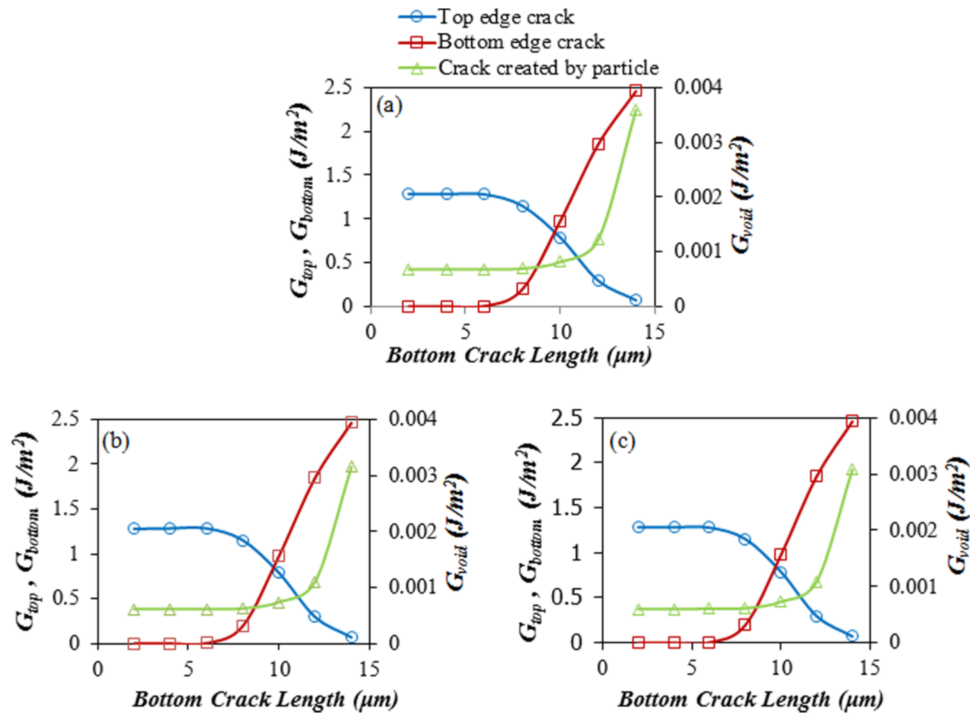

FIG. 7. Interfacial fractures during lift-off; (a) compliant nanoparticle (E ~ 0.2 GPa), (b) semi-rigid nanoparticle (E~10.2 GPa), and (c) rigid nanoparticle (E ~ 70 GPa).

C. Modeling of pull-off as a fracture process

The energy release rates associated with the pull-off stage of cold welding are presented in Figures 7(a)-7(c), for lift-off around compliant nanoparticles (Figure 7(a)), semi-rigid nanoparticles (Figure 7(b)) and rigid nanoparticles (Figure 7(c)). The rigidity of the nanoparticles did not have a significant effect on the energy release rates that were computed for the top edge cracks (Figure 7(a)), bottom edge crack (Figure 7(b)) and the cracks created by the particles (Figure 7(c)). Hence, in all cases, the trends in the computed energy release rates were similar.

In order to understand the implications of the computed energy release rates, it is important to compare the computed results with prior measurements of adhesion energies that were obtained for the relevant bi-material pairs in prior work.[2,27,33,43–45] Prior measurements of adhesion energies are presented Table II and Figure 8. These show that the computed energy release rates (Figure 8) can exceed the measured adhesion energies (Figure 7) obtained in the interfaces that are present in OLED structures.

However, since the crack driving forces are strongly dependent on crack length, initial crack growth for small cracks is more likely to occur along the top edge crack than the bottom (Figure 7). Also, a gradual transition to interfacial crack growth is likely to occur, as the bottom crack length increases beyond ~5 μm (Figure 7). Finally, the voids associated with partial contact around impurities are more likely to induce crack growth, as the bottom crack length increases beyond ~10 μm

TABLE II. Adhesion Energies. Ref. (27 and 38).

Tip Coating	Substrate Coating	Average Force (nN)	Adhesion energy (J/m^2)
Aluminum	MEH-PPV	10.00 ± 1.20	0.8 ± 0.05
MEH-PPV	PEDOT:PSS	59.00 ± 6.00	15.00 ± 3.00
ITO	PEDOT:PSS	30.00 ± 6.70	1.70 ± 0.38
ITO	Glass	58.24 ± 14.33	9.31 ± 1.20

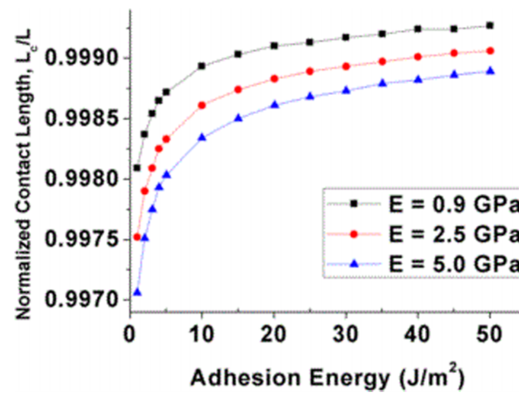

FIG. 8. Adhesion energy against contact length for different Young's moduli (Ref. 27).

(Figure 7). It is important to note that as the crack extends by a kink at the interface, it smoothly follows the interfacial paths of small kink angles for which mode mixities vanishes at all times.[46–50]

D. Dependence of interfacial energy on void or particle height

The dependence of the energy release rate on the initial void length, S, is presented in Figure 9. The results show that the energy release rates decrease with increasing void length. Also, since the void length increases the crack driving forces, increased void lengths are likely to result in higher crack driving forces that are more likely to exceed the interfacial fracture energies (Figure 8 and Table II). Hence, larger voids and partial contacts are more likely to result in favorable conditions for lift-off during cold welding.

E. Implications

The implications of the above results are quite significant for cold welding processes. First, they suggest that cold welding process can be idealized as a two stage process in which the first stage involves evolving contacts with adhesion, while the second stage involves interfacial fracture processes. Since the crack driving forces vary with changes in crack lengths, the initially favored cracks may not be the ones that propagate ultimately to failure.

Furthermore, the conditions for layer cracking may become lower than those required for interfacial cracking in some scenarios.[51–54] In such cases, the cracks may kink in-and-out of interfaces, depending on the prevailing crack driving forces and mode mixities.[25,52,55,56] Such kinking may also

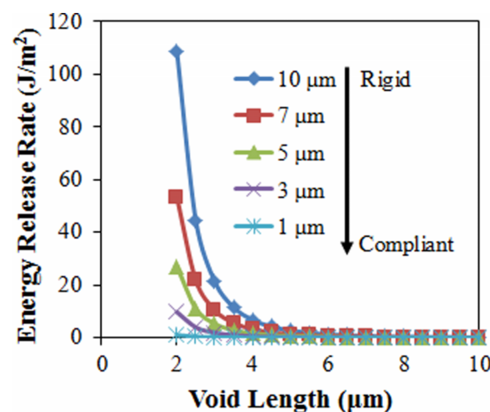

FIG. 9. Effect of dust particle moduli on void length and interfacial energy release rate.

be favored when the microscopic fracture mechanisms (in the layers) favor micro-void coalescence, as shown in prior work by Rahbar *et al.*[57]

In any case, the current work shows that contact, during cold welding, is enhanced by compliant stamps and impurities, applied pressure, and increased adhesion energies. However, increased contact also makes it more difficult for lift-off to occur. Hence, a balance is needed between improved surface contact (for improved charge and light transport[58]) and lift-off for interfacial separation of the stamp from the cold welded structure. This can be facilitated by the use of a layer with low adhesion energy between the stamp and the cold welded layer.[59] Further work is clearly needed to develop process design maps for the design of such low adhesion layers during the contact and lift-off stages of cold welding.

IV. SUMMARY AND CONCLUDING REMARKS

This paper presents the results of a combined analytical and computational study of the contact and lift-off stages associated with the cold welding of Au and Ag thin films. The study shows that the surface contacts improve with increased pressure, reduced film thickness and reduced interfacial nanoparticle stiffness. However, improved contacts result in higher lift-off forces for interfacial separation during the pattern transfer stage of cold welding. Increased pressure may also lead to sink-in of dust particles, which may lead to device damage. An intermediate pressure range is, therefore, needed for the effective cold welding of Au-Au and Au-Ag layers. Also, the analytical model shows that the void length is dependent on the effective modulus and height of the dust particle. The range void sizes observed is similar to the ranges observed in prior experiments on Au-Au[22] and Au-Ag[2] films.

ACKNOWLEDGEMENTS

The authors are grateful to the World Bank STEP-B Program, the African Centers of Excellence Program, the African Capacity Building Foundation, the African Development Bank and the Nelson Mandela Institution and the African University of Science and Technology (AUST) for their financial support. Appreciation is also extended to the scientists and technicians at the Physics Advanced Laboratory at Sheda Science and Technology Complex, Abuja, Nigeria, and Princeton University, New Jersey, USA, for their assistance with experimental techniques.

APPENDIX: ANALYTICAL CALCULATION OF CONTACT LENGTH AS A FUNCTION OF APPLIED PRESSURE FOR COLD WELDING

The surface energy between the film and the substrate is the product of pressure (P), surface contact area ($L_c \times a$) and effective height of the particle $\left(h_{eff}\right)$.[22] This is written as:

$$U_e = -P \times (L_c \times a) \times h = -PahL_c \tag{A1}$$

Since $L_c = L - s$, the total energy in Equation (1) can now be written as:

$$U_s = \frac{6E_{eff}Ih^2}{s^3} - Pah(L - s) \tag{A2}$$

Differentiating Equation (A2) with respect to s gives:

$$\frac{dU_s}{ds} = -\frac{18E_{eff}Ih^2}{s^4} + Pah \tag{A3}$$

The length of the void can be calculated from Equation (A3) at the equilibrium, $dU_s/ds = 0$. This is given by

$$s^4 = \frac{18E_{eff}Ih^2}{Pah} = \frac{18E_{eff}Ih}{Pa}. \tag{A4}$$

Defining the second moment of area as $I = at^3/12$, Equation (A4) can be written as:

$$s = \left(\frac{3E_{eff}t_f^3h}{2P}\right)^{\frac{1}{4}} = L - L_c. \tag{A5}$$

Hence,

$$\frac{L_c}{L} = 1 - \left(\frac{3E_{eff}t_f^3h}{2PL^4}\right)^{\frac{1}{4}}. \tag{A6}$$

Introducing the effective modulus and changing h to h_{eff} gives:

$$\frac{L_c}{L} = 1 - \left(\frac{3\left(\frac{E_dE_f}{E_f\left(1-(\upsilon_d)^2\right)+E_d\left(1-(\upsilon_f)^2\right)}\right)t^3h_{eff}}{2PL^4}\right)^{\frac{1}{4}}. \tag{A7}$$

[1] J.-Y. Lee, S.T. Connor, Y. Cui, and P. Peumans, Nano Lett. **10**, 1276 (2010).
[2] W.O. Akande, Y. Cao, N. Yao, and W. Soboyejo, J. Appl. Phys. **107**, 1 (2010).
[3] Y. Cao, C. Kim, S.R. Forrest, and W. Soboyejo, J. Appl. Phys. **98**, 33713 (2005).
[4] C. Kim, Y. Cao, W.O. Soboyejo, and S.R. Forrest, J. Appl. Phys. **97**, 113512 (2005).
[5] M.B. Tucker, D.R. Hines, and T. Li, J. Appl. Phys. **106**, 103504 (2009).
[6] T.-F. Guo, S. Pyo, S.-C. Chang, and Y. Yang, Adv. Funct. Mater. **11**, 339 (2001).
[7] H. Czichos, J. Phys. D. Appl. Phys. **5**, 1890 (1972).
[8] J. Song and D.J. Srolovitz, J. Mech. Phys. Solids **57**, 776 (2009).
[9] Y. Lu, J.Y. Huang, C. Wang, S. Sun, and J. Lou, Nat. Nanotechnol. **5**, 218 (2010).
[10] J.J. Dumond and H.Y. Low, J. Vac. Sci. Technol. B **30**, 10801 (2012).
[11] A.M. Kendale and D.L. Trumper, US7665983 B2 (2010).
[12] M. Geissler, H. Wolf, R. Stutz, E. Delamarche, U.W. Grummt, B. Michel, and A. Bietsch, Langmuir **19**, 6301 (2003).
[13] A. Bietsch and B. Michel, J. Appl. Phys. **88**, 4310 (2000).
[14] L.M. Campos, T.T. Truong, D.E. Shim, M.D. Dimitriou, D. Shir, I. Meinel, J.A. Gerbec, H.T. Hahn, J.A. Rogers, and C.J. Hawker, Chem. Mater. **21**, 5319 (2009).
[15] C. Kim and S.R. Forrest, Adv. Mater. **15**, 541 (2003).
[16] J. Du, T. Tong, W. Akande, A. Tsakiridou, and W. Soboyejo, Disp. Technol. J. **9**, 601 (2013).
[17] Z. Wang, R. Xing, X. Yu, and Y. Han, Nanoscale **3**, 2663 (2011).
[18] M.M. Ling and Z. Bao, Chem. Mater. **16**, 4824 (2004).
[19] C. Kim, P.E. Burrows, and S.R. Forrest, Science (80-.) **288**, 831 (2000).
[20] D. V Wagle and G.A. Baker, Mater. Horizons (2015).
[21] Z.S. Pereira and E.Z. Da Silva, J. Phys. Chem. C **115**, 22870 (2011).
[22] O.K. Oyewole, D. Yu, J. Du, J. Asare, V.C. Anye, A. Fashina, M.G.Z. Kana, and W.O. Soboyejo, J. Appl. Phys. **118**, 075302 (2015).
[23] Y. Cao, S. Allameh, D. Nankivil, S. Sethiaraj, T. Otiti, and W. Soboyejo, Mater. Sci. Eng. A **427**, 232 (2006).
[24] E.E. Gdoutos and V. Balopoulos, 37 (2010).
[25] M.B. Modi and S.K. Sitaraman, Eng. Fract. Mech. **71**, 1219 (2004).
[26] B. Lauke and T. Schu, **21**, 55 (2001).
[27] D.Y. Momodu, T. Tong, M.G.Z. Kana, A. V Chioh, and W.O. Soboyejo, J. Appl. Phys. **115**, 084504 (2014).
[28] B. Agyei-Tuffour, E.R. Rwenyagila, J. Asare, O.K. Oyewole, M.G.Z. Kana, D.M. O'Carroll, and W.O. Soboyejo, Adv. Mater. Res. **1132**, 204 (2016).
[29] C.H. Mastrangelo and C.H. Hsu, Solid-State Sens. Actuator Work. 5th Tech. Dig. IEEE **212**, 208 (1992).
[30] J.H. Burroughes, D.D.C. Bradley, A.R. Brown, R.N. Marks, K. Mackay, R.H. Friend, P.L. Burns, and A.B. Holmes, Nature **347**, 539 (1990).
[31] F.T. Chiang and J.P. Hung, J. Mech. Sci. Technol. **24**, 1235 (2010).
[32] I.N. Sneddon, Int. J. Eng. Sci. **3**, 47 (1965).
[33] D. Yu, O.K. Oyewole, D. Kwabi, T. Tong, V.C. Anye, J. Asare, E. Rwenyagila, A. Fashina, O. Akogwu, J. Du, and W.O. Soboyejo, J. Appl. Phys. **116**, 074506 (2014).
[34] G. Wei, B. Bhushan, and S. Joshua Jacobs, Ultramicroscopy **100**, 375 (2004).
[35] O.K. Oyewole, D. Yu, J. Du, J. Asare, D.O. Oyewole, V.C. Anye, A. Fashina, M.G.Z. Kana, and W.O. Soboyejo, J. Appl. Phys. **117**, 235501 (2015).
[36] N. Bowden, S. Brittain, A.G. Evans, J.W. Hutchinson, and G.M. Whitesides, Nature **393**, 146 (1998).
[37] D.G. Neerinck and T.J. Vink, Thin Solid Films **278**, 12 (1996).
[38] W. Soboyejo, *Mechanical Properties of Engineered Materials* (Marcel Dekker, Inc, New York, NY, 2003).
[39] L.J. Gibson, M.F. Ashby, G.N. Karam, U. Wegst, and H.R. Shercliff, The Royal Society **450** (1995).

[40] V. Raghavan, *Material Science and Engineering*, 4th ed. (Prentice Hall of India Ltd, 1994).
[41] PeriodicTable.com, Math. Elem. Funct. from Wolfram Res. Inc. (2006).
[42] PeriodicTable.com, Math. Elem. Funct. from Wolfram Res. Inc. (2016).
[43] S.R. Dupont, E. Voroshazi, P. Heremans, and R.H. Dauskardt, Org. Electron. Physics, Mater. Appl. **14**, 1262 (2013).
[44] T. Tong, B. Babatope, S. Admassie, J. Meng, O. Akwogu, W. Akande, and W.O. Soboyejo, J. Appl. PHYSICS, Am. Inst. Phys. **106**, 1 (2009).
[45] H.R. Brown, IBM J. Res. Dev. **38**, 379 (1994).
[46] F. Erdogan and G.C. Sih, J. Basic Eng. **85**, 519 (1963).
[47] K.B. Broberg, Eng. Fract. Mech. **28**, 663 (1987).
[48] J.F. Kalthoff, *Proc. an Int. Conf. Dyn. Crack Propag.* (1973), pp. 449–458.
[49] H. Bergkvist and L. Guex, Int. J. Fract. **15**, 429 (1979).
[50] J. Gunnars, P. Stahle, and T.C. Wang, Comput. Mech. Springer **19**, 545 (1997).
[51] P. Qiao and J. Wang, Int. J. Solids Struct. **41**, 7423 (2004).
[52] J.W. Hutchinson and Z. Suo, Adv. Appl. Mech. **29**, 191 (1992).
[53] Z. Suo and J.W. Hutchinson, Int. J. Fract. **43**, 1 (1990).
[54] J. Wang and P. Qiao, J. Mech. Phys. Solids **52**, 891 (2004).
[55] R.C. Ostergaard, B.F. Sorensen, and P. Brondsted, J. Sandw. Struct. Mater. **9**, 445 (2007).
[56] S. Liu, Y. Mei, and T.Y. Wu, Components, Packag. Manuf. Technol. Part A, IEEE Trans. **18**, 618 (1995).
[57] N. Rahbar, Y. Yang, and W. Soboyejo, Mater. Sci. Eng. A **488**, 381 (2008).
[58] J. Cui, Q. Huang, Q. Wang, and T.J. Marks, Langmuir **17**, 2051 (2001).
[59] D. Hegemann, H. Brunner, and C. Oehr, Nucl. Instruments Methods Phys. Res. Sect. B Beam Interact. with Mater. Atoms **208**, 281 (2003).